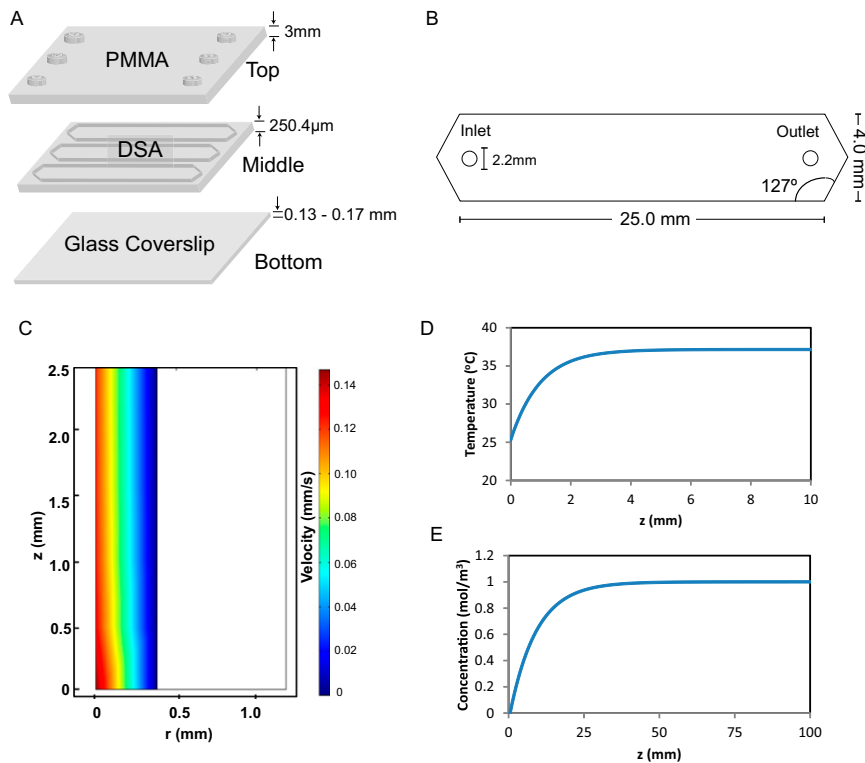# Supporting Information

## Rizvi et al. 10.1073/pnas.1216989110

Fig. S1. Components and fabrication of microfluidic channels (*A* and *B*) and computational modeling of thermal and gaseous equilibration along a porous silicone tubing during culture medium flow (*C–E*). (*A*) Microfluidic channels are composed of three components: a coverslip, a micromachined double-sided adhesive (DSA) layer with embedded channels, and the top polymethylmethacrylate (PMMA) layer with micromachined inlet and outlet ports. (*B*) The dimensions of an individual channel. (*C*) Velocity contours (mm/s) of medium flowing inside the porous silicone tube on the axisymmetric layer. (*D*) Temperature (°C), and (*E*) CO_2 concentrations (moles/m^3) are plotted as a function of length (millimeter) at $r = 0$, along the axisymmetric line.
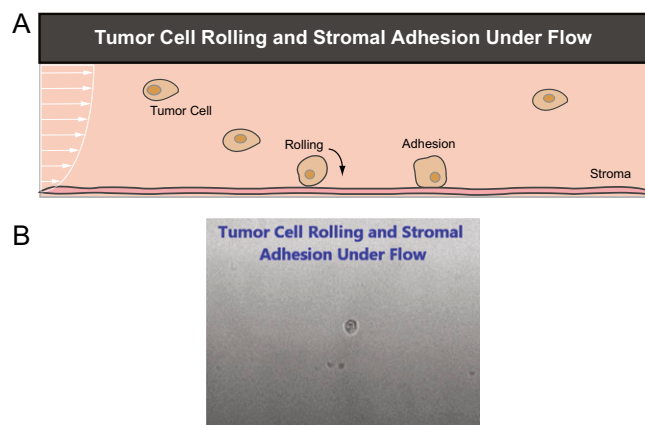
Fig. S2. (*A*) Under the influence of flow, a portion of the tumor cells that enter the microfluidic channel will roll along, and adhere to, stromal beds. Other cells fail to adhere or remain in the fluidic stream, and eventually exit the channel. (*B*) A still image from Movie S1 showing an ovarian cancer cell in a microfluidic channel adhered to a Matrigel bed.
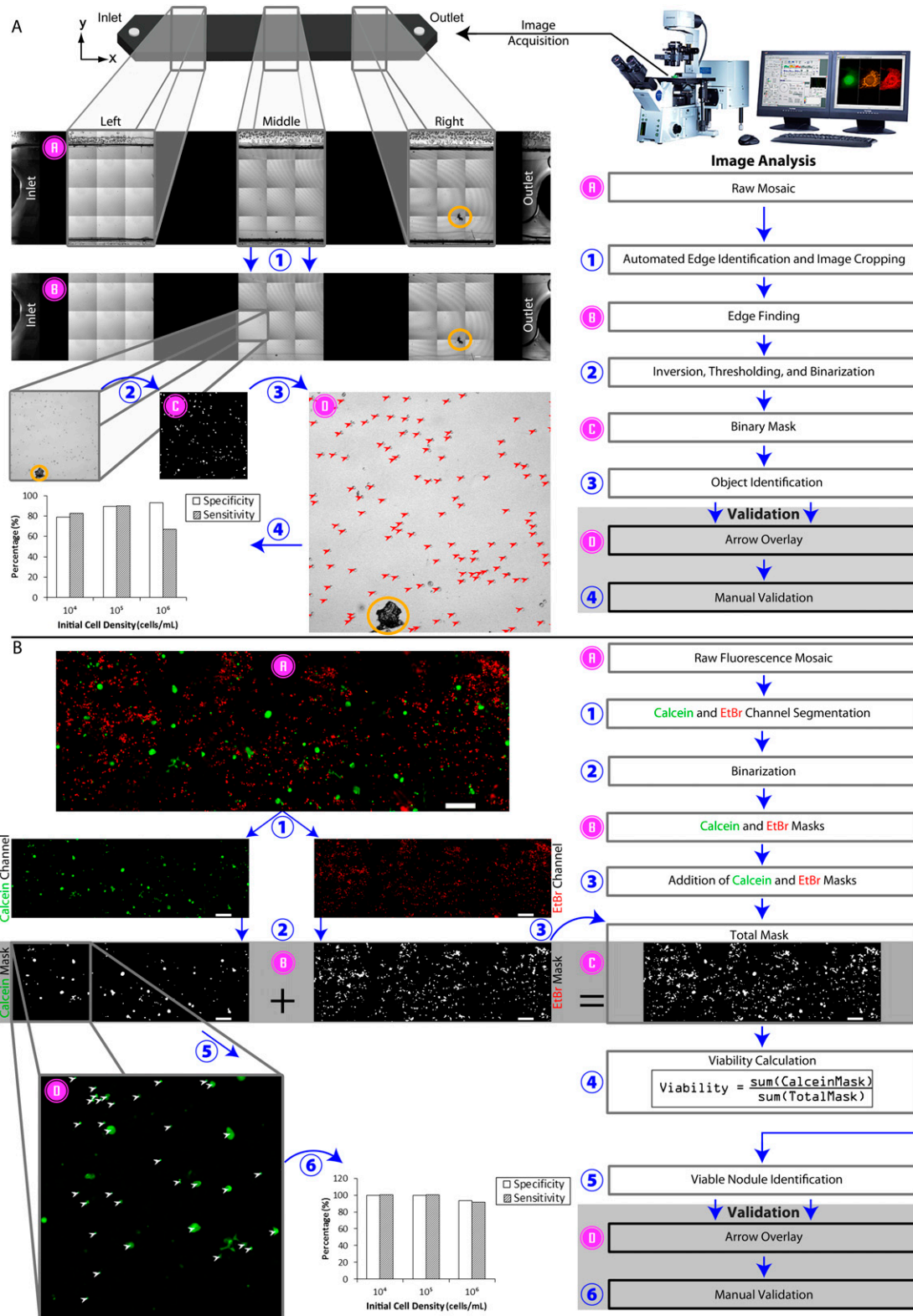
Fig. S3. An overview of image processing and analysis for (*A*) brightfield and (*B*) live–dead fluorescence images of microfluidic channels collected via confocal microscopy. Items numbered in blue represent processes in image analysis; items lettered in pink represent outcomes. For example, step 1 in brightfield image processing is to find the edges in the raw mosaic (item A) and then crop the image to obtain the trimmed, edge-found result (item B). Analysis of brightfield images in *A* ultimately results in object identification, which is validated manually via arrow overlays (steps 3 and 4). Sensitivity and specificity values are >85% at all seeding densities except 10^6 cells/mL. At this density, sensitivity decreases because the presence of large clusters of closely packed cells makes it difficult for the algorithm to distinguish them from noncellular artifacts. The orange circles present in *A* highlight large chunks of cellular debris that were rejected by the algorithm based on their large area and irregular shape. Live–dead fluorescence images in *B* are used for quantitative viability assessment (steps 1–4) as well as viable nodule identification, which also is manually validated here (steps 5 and 6). Sensitivity and specificity are reported for all densities.
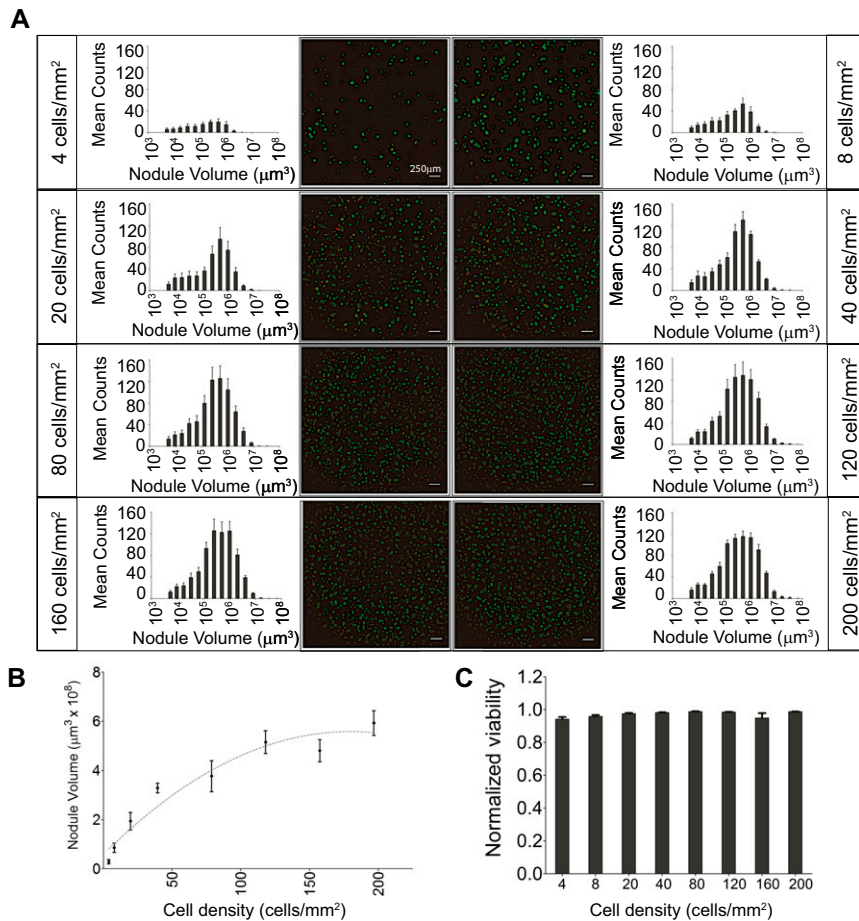
Fig. S4. Tumor volumes and viabilities of ovarian cancer micronodules after 7 d of growth in traditional nonflow 3D cultures. (*A*) Micronodule formation was observed at all plating densities ranging from 4 cells/mm^2 to 200 cells/mm^2. The volume distribution of micronodules shifted toward larger nodule volumes with increasing plating density. (*B*) Total 3D nodule volume increased exponentially with increasing plating density ($R^2 = 0.7776$). (*C*) Tumor viability was >97% across all plating densities in traditional nonflow conditions. Viabilities were internally normalized to total fluorescence [calcein (live cells) plus ethidium (dead cells)] for each plating density. Initial cell concentrations for nonflow cultures were chosen based on the densities of adherent cells detected immediately after flow, as shown in Fig. 3 *B* and *G–I*.

Movie S1. An ovarian cancer cell in a microfluidic channel rolling, then adhering and stopping on a Matrigel bed under the influence of flow. This cell is representative of the population of tumor cells that may grow into aggressive 3D nodules due to the effects of continuous flow in the microfluidic channels, as described in the present study.

Movie S1